SCIENCE CHINA
Physics, Mechanics & Astronomy

• Article •
Special Topic: Microscopic Mechanism for Manipulating Thermal Conduction

November 2022 Vol. 65 No. 11: 117007
https://doi.org/10.1007/s11433-021-1889-5

Breaking efficiency limit of thermal concentrators by conductivity couplings

Pengfei Zhuang[1], Liujun Xu[1*], Peng Tan[2*], Xiaoping Ouyang[3], and Jiping Huang[1*]

[1] *Department of Physics, State Key Laboratory of Surface Physics, and Key Laboratory of Micro and Nano Photonic Structures (MOE), Fudan University, Shanghai 200438, China;*
[2] *Department of Physics and State Key Laboratory of Surface Physics, Fudan University, Shanghai 200438, China;*
[3] *School of Materials Science and Engineering, Xiangtan University, Xiangtan 411105, China*

Received December 19, 2021; accepted March 11, 2022; published online September 1, 2022

The concentrating efficiency of a thermal concentrator can be reflected in the ratio of its interior to exterior temperature gradients, which, however, has an upper limit in existing schemes. Here, we manage to break this upper limit by considering the couplings of thermal conductivities and improve the concentrating efficiency of thermal concentrators. For this purpose, we first discuss a monolayer scheme with an isotropic thermal conductivity, which can break the upper limit but is still restricted by its geometric configuration. To go further, we explore another degree of freedom by considering the monolayer scheme with an anisotropic thermal conductivity or by adding the second shell with an isotropic thermal conductivity, thereby making the concentrating efficiency completely free from the geometric configuration. Nevertheless, apparent negative thermal conductivities are required, and we resort to external heat sources realizing the same effect without violating the second law of thermodynamics. Finite-element simulations are performed to confirm the theoretical predictions, and experimental suggestions are also provided to improve feasibility. These results may have potential applications for thermal camouflage and provide guidance to other diffusive systems such as static magnetic fields and dc current fields for achieving similar behaviors.

thermal concentrator, concentrating efficiency, conductivity coupling, apparent negative conductivity

PACS number(s): 44.10.+i, 05.70.-a, 81.05.Zx

Citation: P. Zhuang, L. Xu, P. Tan, X. Ouyang, and J. Huang, Breaking efficiency limit of thermal concentrators by conductivity couplings, Sci. China-Phys. Mech. Astron. **65**, 117007 (2022), https://doi.org/10.1007/s11433-021-1889-5

1 Introduction

The theory of transformation thermotics [1-3] has promoted an advanced control of heat transfer based on thermal metamaterials [4-7]. As a representative example, a thermal concentrator [8-31] can increase its interior temperature gradient without distorting its exterior one. So far, many schemes have been proposed to design thermal concentrators. The initial explorations are based on the theory of transformation thermotics [8-21] which is a bridge linking space transformations and material transformations. Therefore, the effect of thermal concentrating can be achieved by coating a region (i.e., the core) with a designed shell (i.e., the thermal concentrator). This scheme has three features: (1) the thermal conductivities inside and outside the shell are identical; (2) the shell has an anisotropic thermal conductivity that is commonly realized by a lay-

*Corresponding authors (Liujun Xu, email: 13307110076@fudan.edu.cn; Peng Tan, email: tanpeng@fudan.edu.cn; Jiping Huang, email: jphuang@fudan.edu.cn)

ered structure [22-26]; and (3) both temperature gradient and heat flux are enhanced in the core. An alternative scheme is based on the effective medium theory [27-29, 32-34] with also three features: (1) the thermal conductivity inside the shell should be smaller than that outside the shell; (2) the shell requires only a homogeneous and isotropic thermal conductivity; and (3) temperature gradient increases but heat flux decreases in the core. Recently, topology optimization has also become a powerful tool to design thermal concentrators [30, 31], which largely reduces the requirements for materials and structures [35-40].

Despite varieties of schemes, the concentrating efficiency of a thermal concentrator, commonly reflected in the ratio of its interior to exterior temperature gradients, has an upper limit. Specifically, when a circular concentrator with inner radius r_c and outer radius r_s is designed, the upper limit for the concentrating efficiency is $\eta = r_s/r_c$ [8-33], indicating that the isotherms in the shell are completely compressed to the core. To reach the upper limit, the theory of transformation thermotics requires to design a shell with an extremely anisotropic thermal conductivity [41-45], and the effective medium theory needs to fabricate a core with a near-zero thermal conductivity [27-29]. However, it is still challenging to break the upper limit for the concentrating efficiency.

To solve the problem, here we investigate a monolayer scheme and two extended schemes with the couplings of thermal conductivities. All these three schemes feature the simultaneous concentrating of heat flux and temperature gradient with only homogeneous materials. More importantly, they also contribute to the much higher concentrating efficiency than existing schemes, including traditional thermal concentrators based on transformation thermotics, the effective medium theory, topology optimization, etc. Nevertheless, apparent negative thermal conductivities are required, which can be effectively realized with external heat energy and have been applied to design thermal metamaterials [46-50].

2 Monolayer scheme with an isotropic thermal conductivity

We first discuss a monolayer scheme in the Cartesian coordinate system x_i ($i = 1, 2, 3$ for three dimensions and $i = 1, 2$ for two dimensions). A confocal core-shell structure is embedded in a background (Figure 1(a)). The semi-axis of the core (or shell) along the x_i axis is denoted as r_{ci} (or r_{si}). The thermal conductivities of the core, shell, and background are denoted as κ_c, κ_s, and κ_b, respectively. The conversion between the Cartesian coordinates x_i and elliptical (or ellipsoidal) coordinates ρ_j is

$$\sum_i \frac{x_i^2}{\rho_j + r_{ci}^2} = 1 \tag{1}$$

with parameters of $j = 1, 2, 3$ for three dimensions and $j = 1, 2$ for two dimensions.

In particular, the coordinate ρ_1 ($> -r_{ci}^2$) plays the role that the radius plays in spherical coordinates. For example, the inner and outer boundaries of the shell can be denoted as $\rho_1 = \rho_c$ ($= 0$) and $\rho_1 = \rho_s$, respectively. In the presence of a uniform thermal field along the x_i axis, thermal conduction equation can be expressed in the elliptical (or ellipsoidal) coordinate system as [51]:

$$\frac{\partial}{\partial \rho_1}\left[g(\rho_1)\frac{\partial T}{\partial \rho_1}\right] + \frac{g(\rho_1)}{\rho_1 + r_{ci}^2}\frac{\partial T}{\partial \rho_1} = 0, \tag{2}$$

with a definition of $g(\rho_1) = \prod_i \left(\rho_1 + r_{ci}^2\right)^{1/2}$. For three dimensions, $4\pi g(\rho_1 = 0)/3 = 4\pi r_{c1}r_{c2}r_{c3}/3$ (or $4\pi g(\rho_1 = \rho_s)/3 = 4\pi r_{s1}r_{s2}r_{s3}/3$) represents the volume of the core (or the core plus the shell). For two dimensions, $\pi g(\rho_1 = 0) = \pi r_{c1}r_{c2}$ (or $\pi g(\rho_1 = \rho_s) = \pi r_{s1}r_{s2}$) denotes the area of the core (or the core plus the shell). The temperature distributions along the x_i axis in the core T_{ci}, shell T_{si}, and background T_{bi} can be expressed as [51]:

$$\begin{cases} T_{ci} = A_{ci}x_i, \\ T_{si} = \left[A_{si} + B_{si}\phi_i(\rho_1)\right]x_i, \\ T_{bi} = \left[A_{bi} + B_{bi}\phi_i(\rho_1)\right]x_i, \end{cases} \tag{3}$$

with a definition of $\phi_i(\rho_1) = \int_{\rho_c}^{\rho_1}\left[\left(\rho_1 + r_{ci}^2\right)g(\rho_1)\right]^{-1}\mathrm{d}\rho_1$. A_{ci}, A_{si}, B_{si}, and B_{bi} can be determined by the continuities of temperature and normal heat flux (see sect. A1 of Appendix). Since the temperature distribution in the background should

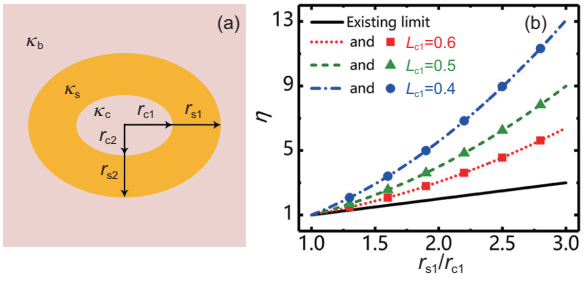

Figure 1 (Color online) (a) Monolayer scheme with an isotropic thermal conductivity. (b) Concentrating efficiency η as a function of geometric configuration r_{s1}/r_{c1}. Lines and points denote theoretical results and simulation results, respectively. The geometric parameters (r_{c1}, r_{c2}, r_{s1}, and r_{s2}) of a thermal concentrator are determined by L_{c1} and r_{s1}/r_{c1} (see eq. (a7) in sect. A1 of Appendix)

be undistorted, we take $B_{bi}=0$ and then obtain

$$\kappa_b=\frac{L_{ci}\kappa_c+(1-L_{ci})\kappa_s+(1-L_{si})(\kappa_c-\kappa_s)f}{L_{ci}\kappa_c+(1-L_{ci})\kappa_s-L_{si}(\kappa_c-\kappa_s)f}\kappa_s, \tag{4}$$

with a definition of $f=g(\rho_c)/g(\rho_s)=\prod_i r_{ci}/r_{si}$. The shape factor (see eqs. (a3) and (a4) in sect. A1 of Appendix) L_{ci} (or L_{si}) reflects the flattening degree of the ellipse. For two dimensions, the shape factors can be written as $L_{w1}=r_{w2}/(r_{w1}+r_{w2})$ and $L_{w2}=r_{w1}/(r_{w1}+r_{w2})$, where w can take c or s. The further the shape factor is away from 0.5, the more flattening the ellipse is.

Therefore, the concentrating efficiency of a thermal concentrator can then be defined as the ratio of its interior and exterior temperature gradients (taking $B_{bi}=0$),

$$\eta=\frac{\nabla T_{ci}}{\nabla T_{bi}}=\frac{A_{ci}}{A_{bi}}=\frac{\kappa_s}{L_{ci}\kappa_c+(1-L_{ci})\kappa_s-L_{si}(\kappa_c-\kappa_s)f}. \tag{5}$$

For a two-dimensional circular case with $L_{ci}=L_{si}=1/2$, eq. (5) can be reduced to

$$\eta=\frac{2\kappa_s}{\kappa_c+\kappa_s-(\kappa_c-\kappa_s)f}. \tag{6}$$

For a three-dimensional spherical case with $L_{ci}=L_{si}=1/3$, eq. (5) can be reduced to

$$\eta=\frac{3\kappa_s}{\kappa_c+2\kappa_s-(\kappa_c-\kappa_s)f}. \tag{7}$$

We also consider the same thermal conductivities inside and outside the shell and then obtain two coupling conditions to satisfy $\kappa_c=\kappa_b$,

$$\kappa_s=\kappa_c, \tag{8}$$

$$-\frac{1-L_{ci}-(1-L_{si})f}{L_{ci}-L_{si}f}\kappa_s=\kappa_c. \tag{9}$$

Eq. (8) leads to a trivial case with $\kappa_c=\kappa_s=\kappa_b$ and $\eta=1$. However, if we apply the coupling condition described by eq. (9), the concentrating efficiency largely increases,

$$\eta=f^{-1}=\prod_i r_{si}/r_{ci}. \tag{10}$$

Clearly, the concentrating efficiency exceeds the upper limit for existing thermal concentrators $\eta=r_{s1}/r_{c1}$, and a smaller L_{c1} yields a larger η (Figure 1(b)). However, the concentrating efficiency is still restricted by the geometric configuration, so we further consider the following two schemes by adding another degree of freedom.

3 Monolayer scheme with an anisotropic thermal conductivity

In this section, we consider a shell with an anisotropic thermal conductivity. Since it is not convenient to unify two and three dimensions, we independently discuss them. Nevertheless, the conclusion of three dimensions is similar to that of two dimensions. We first discuss a two-dimensional circular shell with inner and outer radii of r_c and r_s, respectively (Figure 2(a)). The thermal conduction equation can be written in the cylindrical coordinate system (r,θ) as [41]:

$$\frac{1}{r}\frac{\partial}{\partial r}\left(r\kappa_{srr}\frac{\partial T}{\partial r}\right)+\frac{1}{r}\frac{\partial}{\partial\theta}\left(\kappa_{s\theta\theta}\frac{\partial T}{r\partial\theta}\right)=0, \tag{11}$$

where κ_{srr} and $\kappa_{s\theta\theta}$ are the radial and tangential thermal conductivities of the shell, respectively. The temperature distributions of the core T_c, shell T_s, and background T_b can be written as [41]:

$$\begin{cases}T_c=A_c r\cos\theta,\\ T_s=\left(A_s r^{d_{s1}}+B_s r^{d_{s2}}\right)\cos\theta,\\ T_b=\left(A_b r+B_b r^{-1}\right)\cos\theta,\end{cases} \tag{12}$$

with definitions of $d_{s1}=\sqrt{\kappa_{s\theta\theta}/\kappa_{srr}}$ and $d_{s2}=-\sqrt{\kappa_{s\theta\theta}/\kappa_{srr}}$. A_c, A_s, B_s, and B_b are four constants to be determined by the boundary conditions (see sect. A2 of Appendix). By taking $B_b=0$, we can further derive

$$\kappa_b=\frac{d_{s1}(\kappa_c-d_{s2}\kappa_{srr})-d_{s2}(\kappa_c-d_{s1}\kappa_{srr})f^{(d_{s1}-d_{s2})/2}}{\kappa_c-d_{s2}\kappa_{srr}-(\kappa_c-d_{s1}\kappa_{srr})f^{(d_{s1}-d_{s2})/2}}\kappa_{srr}, \tag{13}$$

with a definition of $f=r_c^2/r_s^2$. We also define the concentrating efficiency as:

$$\eta=\frac{A_c}{A_b}=\frac{(d_{s1}-d_{s2})\kappa_{srr}f^{(d_{s1}-1)/2}}{\kappa_c-d_{s2}\kappa_{srr}-(\kappa_c-d_{s1}\kappa_{srr})f^{(d_{s1}-d_{s2})/2}}. \tag{14}$$

For an isotropic case with $d_{s1}=-d_{s2}=1$, eq. (14) can be simplified as:

$$\eta=\frac{2\kappa_{srr}}{\kappa_c+\kappa_{srr}-(\kappa_c-\kappa_{srr})f}, \tag{15}$$

which has the same form as eq. (6) in sect. 2.

We also obtain two coupling conditions for $\kappa_c=\kappa_b$,

$$d_{s1}\kappa_{srr}=\kappa_c, \tag{16}$$

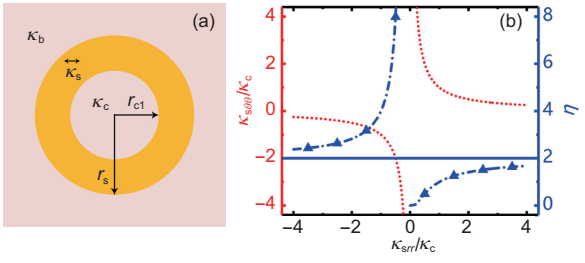

Figure 2 (Color online) (a) Monolayer scheme with an anisotropic thermal conductivity. (b) $\kappa_{s\theta\theta}/\kappa_c$ and η as a function of κ_{srr}/κ_c when $r_s/r_c=2$. Lines and points denote theoretical results and simulation results, respectively.

$$d_{s2}\kappa_{srr} = \kappa_c. \tag{17}$$

Eqs. (16) and (17) can be unified as:

$$\kappa_{srr}\kappa_{s\theta\theta} = \kappa_c^2, \tag{18}$$

which is plotted with the dotted line in Figure 2(b).

When the thermal conductivities of the core and shell satisfy eq. (18), eq. (14) becomes

$$\eta = f^{-(1-\kappa_c/\kappa_{srr})/2} = (r_s/r_c)^{1-\kappa_c/\kappa_{srr}}, \tag{19}$$

which is plotted with the dashed-dotted line in Figure 2(b). When $\kappa_{srr}/\kappa_c \to 0^+$, heat flow bypasses the core, resulting in the uniform temperature in the core and $\eta \to 0$. Nevertheless, the shell plays a different role when κ_{srr}/κ_c is negative because there is a circumfluence (see the discussion in sect. 6) between the core and the shell. As $\kappa_{srr}/\kappa_c \to 0^-$, most heat flow goes from the cold end of the core back to the hot end of the core (through the shell), thereby leading to $\eta \to \infty$. Moreover, we can observe $\eta \to r_s/r_c$ when $\kappa_{srr}/\kappa_c \to \pm\infty$, which is just the upper limit for existing concentrating efficiency (see the solid line in Figure 2(b)). If the thermal conductivity of the shell is isotropic and nontrivial $\kappa_{srr}/\kappa_c = 1/d_{s2} = -1$, the concentrating efficiency also exceeds the upper limit and becomes $\eta = r_s^2/r_c^2$, which is in accordance with the two-dimensional conclusion in sect. 2. Therefore, the concentrating efficiency can exceed the upper limit and even approach infinity when $\kappa_{srr}/\kappa_c \to 0^-$. The two-dimensional conclusion can also be extended to three dimensions, which is discussed in sect. A3 of Appendix.

4 Bilayer scheme with isotropic thermal conductivities

In this section, we consider the second shell whose isotropic thermal conductivity and semi-axis along the x_i axis are denoted as κ_t and r_{ti}, respectively (Figure 3(a)). With the conclusion of the monolayer scheme (i.e., eq. (4)), the effective thermal conductivity of the core and the first shell κ_{cs} can be calculated by

$$\kappa_{cs} = \frac{L_{ci}\kappa_c + (1-L_{ci})\kappa_s + (1-L_{si})(\kappa_c-\kappa_s)f}{L_{ci}\kappa_c + (1-L_{ci})\kappa_s - L_{si}(\kappa_c-\kappa_s)f}\kappa_s. \tag{20}$$

We then treat the core and the first shell as an effective core with an effective thermal conductivity of κ_{cs}, so we can further derive

$$\kappa_b = \frac{L_{si}\kappa_{cs} + (1-L_{si})\kappa_t + (1-L_{ti})(\kappa_{cs}-\kappa_t)p}{L_{si}\kappa_{cs} + (1-L_{si})\kappa_t - L_{ti}(\kappa_{cs}-\kappa_t)p}\kappa_t, \tag{21}$$

with a definition of $p = g(\rho_s)/g(\rho_t) = \prod_i r_{si}/r_{ti}$. ρ_t denotes the outer boundary of the second shell. L_{ti} is the shape factor of the second shell along the x_i axis,

$$L_{ti} = \frac{g(\rho_t)}{2}\int_{\rho_t}^{\infty}\left[\left(\rho_1 + r_{ci}^2\right)g(\rho_1)\right]^{-1} d\rho_1. \tag{22}$$

We can also express the concentrating efficiency as:

$$\eta = \frac{A_{ci}}{A_{bi}} = \frac{\kappa_s\kappa_t}{\lambda_1+\lambda_2+\lambda_3}, \tag{23}$$

where λ_1, λ_2, and λ_3 take the form of

$$\begin{cases} \lambda_1 = [L_{ci}\kappa_c + (1-L_{ci})\kappa_s] \\ \qquad \times [L_{si}\kappa_s + (1-L_{si})\kappa_t - L_{ti}(\kappa_s-\kappa_t)p], \\ \lambda_2 = -L_{ti}(\kappa_c-\kappa_s)[(1-L_{si})\kappa_s + L_{si}\kappa_t]fp, \\ \lambda_3 = L_{si}(1-L_{si})(\kappa_c-\kappa_s)(\kappa_s-\kappa_t)f. \end{cases} \tag{24}$$

As a more general model, the bilayer scheme can also be reduced to the monolayer scheme in sect. 2 at two certain conditions. When $\kappa_c = \kappa_s$, eq. (23) can be simplified as:

$$\eta = \frac{\kappa_t}{L_{si}\kappa_s + (1-L_{si})\kappa_t - L_{ti}(\kappa_s-\kappa_t)p}. \tag{25}$$

When $\kappa_s = \kappa_t$, eq. (23) becomes

$$\eta = \frac{\kappa_t}{L_{ci}\kappa_c + (1-L_{ci})\kappa_t - L_{ti}(\kappa_c-\kappa_t)fp}. \tag{26}$$

Obviously, eqs. (25) and (26) have similar forms as eq. (5) in sect. 2.

We can also derive two coupling conditions for $\kappa_c = \kappa_b$,

$$M(\kappa_s, \kappa_t) = \kappa_c, \tag{27}$$

$$N(\kappa_s, \kappa_t) = \kappa_c. \tag{28}$$

M and N are two analytical functions. Therefore, one κ_t corresponds to two κ_s for satisfying $\kappa_c = \kappa_b$, i.e., $\kappa_s = m(\kappa_t)$ being a continuous function (see the dotted line in the upper inset of Figure 3(b)) and $\kappa_s = n(\kappa_t)$ being a quasi-hyperbolic function (see the dotted line in the lower inset of Figure 3(b)). We do not express the concrete forms of m and n because they are too complicated.

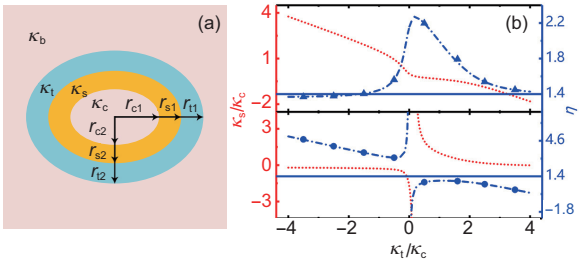

Figure 3 (Color online) (a) Bilayer scheme with isotropic thermal conductivities. (b) κ_s/κ_c and η as a function of κ_t/κ_c when $r_{s1}/r_{c1} = 1.2$, $r_{t1}/r_{c1} = 1.4$, and $L_{c1} = 1/3$. Lines and points denote theoretical results and simulation results, respectively.

When eq. (27) is satisfied, the upper limit of $\eta = r_{t1}/r_{c1}$ can be broken, but the concentrating efficiency can still not tend to infinity (see the dashed-dotted line in the upper inset of Figure 3(b)). Moreover, eq. (27) contains two special cases that can be reduced to the conclusion in sect. 2. One features a concentrating efficiency of $\eta = f^{-1}$ with the same thermal conductivities of the second shell and core,

$$-\frac{1-L_{ci}-(1-L_{si})f}{L_{ci}-L_{si}f}\kappa_s = \kappa_t = \kappa_c. \tag{29}$$

The other features a concentrating efficiency of $\eta = p^{-1}$ with the same thermal conductivities of the first shell and core,

$$\kappa_s = -\frac{1-L_{si}-(1-L_{ti})p}{L_{si}-L_{ti}p}\kappa_t = \kappa_c. \tag{30}$$

Fortunately, eq. (28) can lead to an infinite efficiency. $\kappa_t/\kappa_c \to 0^-$ and $\kappa_t/\kappa_c \to 0^+$, respectively, yield $\eta \to \infty$ and $\eta \to -\infty$, and the thermal conductivity of the first shell satisfies

$$-\frac{1-L_{ci}-(1-L_{si})f}{L_{ci}+(1-L_{si})f}\kappa_s \approx \kappa_c. \tag{31}$$

Meanwhile, $\kappa_t/\kappa_c \to \mp\infty$ can also lead to $\eta \to \pm\infty$, and the thermal conductivity of the first shell satisfies

$$-\frac{1-L_{ci}+L_{si}f}{L_{ci}-L_{si}f}\kappa_s \approx \kappa_c. \tag{32}$$

Moreover, eq. (28) also contains a special case that can be reduced to the conclusion in sect. 2. That is, the concentrating efficiency of $\eta = (fp)^{-1}$ occurs when the two shells have the same thermal conductivities,

$$\begin{aligned}\kappa_c &= -\frac{1-L_{ci}-(1-L_{ti})fp}{L_{ci}-L_{ti}fp}\kappa_s \\ &= -\frac{1-L_{ci}-(1-L_{ti})fp}{L_{ci}-L_{ti}fp}\kappa_t.\end{aligned} \tag{33}$$

There is another case for $\eta = (fp)^{-1}$ if the thermal conductivities of the two shells satisfy

$$\begin{aligned}\kappa_c &= -\frac{1-L_{ci}-(1-L_{si})f}{L_{ci}-L_{si}f}\kappa_s \\ &= -\frac{1-L_{si}-(1-L_{ti})p}{L_{si}-L_{ti}p}\kappa_t.\end{aligned} \tag{34}$$

Conductivity coupling occurs layer by layer in this case. The core is coupled with the first shell described by eq. (9). Then, they are treated as an effective core with an effective thermal conductivity of κ_c. The effective core is then coupled with the second shell described by the similar form of eq. (9).

Another unique feature of eq. (28) is the concentrating efficiency of $\eta < 0$ when the thermal conductivity of the second shell satisfies

$$\kappa_t > \frac{1-L_{si}+L_{ti}p}{1-L_{si}-(1-L_{ti})p}\kappa_c, \tag{35}$$

or

$$0 < \kappa_t < \frac{L_{si}-L_{ti}p}{L_{si}+(1-L_{ti})p}\kappa_c, \tag{36}$$

indicating that the temperature gradient in the core changes its direction.

Then we can draw a brief conclusion for these three schemes. The monolayer scheme with an isotropic thermal conductivity can break the upper limit but is still restricted by its geometric configuration. To be free from geometric configurations, we further consider the monolayer scheme with an anisotropic thermal conductivity and the bilayer scheme with isotropic thermal conductivities. For the former, the efficiency can tend to infinity with $\kappa_{srr}/\kappa_c \to 0^-$. For the latter, the efficiency can also reach infinity when $\kappa_t/\kappa_c \to 0^-$ or $\kappa_t/\kappa_c \to -\infty$. Moreover, the latter features $\eta < 0$ if the coupling condition is appropriately chosen.

5 Finite-element simulations of thermal concentrators

We also perform finite-element simulations to confirm the theories with COMSOL Multiphysics (http://www.comsol.com/). From a practical perspective, although interfacial thermal resistance exists widely [52-54], its effect at the macroscopic scale is not dominant so it is reasonable to ignore it. Without loss of generality, we consider a two-dimensional case with size 10 cm×10 cm and set the thermal conductivities of the core and background as 1 W m^{-1} K^{-1}. The left boundaries are set at 313 K, the right boundaries are set at 273 K, and both the upper and lower boundaries are adiabatic. To quantitatively compare the concentrating efficiency of different thermal concentrators, we introduce a dimensionless temperature of $T^* = 100(T - T_0)/T_0$ and a dimensionless position of $x^* = x/w$, where T_0 and w denote the central temperature and half-length of the system, respectively.

Thermal concentrating aims to increase the temperature gradient in the core without distorting that in the background. In order to confirm eqs. (5), (8), and (9) and demonstrate the expected case shown in Figure 1, we design three structures with different shape factors, and the corresponding results are presented in Figure 4(a)-(c). The temperature profiles outside the shells are undistorted as if there was not core-shell structures in the center. Meanwhile, the isotherms in the cores are concentrated as expected. According to the Fourier law $\boldsymbol{J} = -\kappa\nabla T$, heat fluxes are also enhanced in the cores due to the larger temperature gradients. The dimensionless temperatures are plotted as a function of dimensionless position in Figure 4(d).

By considering the monolayer scheme with an anisotropic thermal conductivity, we confirm the theoretical prediction of eqs. (14) and (17). Then, we design three structures with different thermal conductivities of the shells (Figure 5(a)-(c)). Similar to Figure 4, the temperature profiles in Figure 5(a)-(c) prove the effect of thermal concentrating. Also, we draw the temperature distribution of a thermal concentrator (Figure 5(d)) designed by transformation theory for comparison. Figure 5(e) displays the temperature distribution along the central horizontal axis. As presented in Figure 2(b), the temperature gradient in the core increases with the increment of κ_{srr}/κ_c, leading to the improvement of concentrating efficiency. Thus, we can control $\kappa_{srr}/\kappa_c \to 0^-$ for an extreme concentrating efficiency.

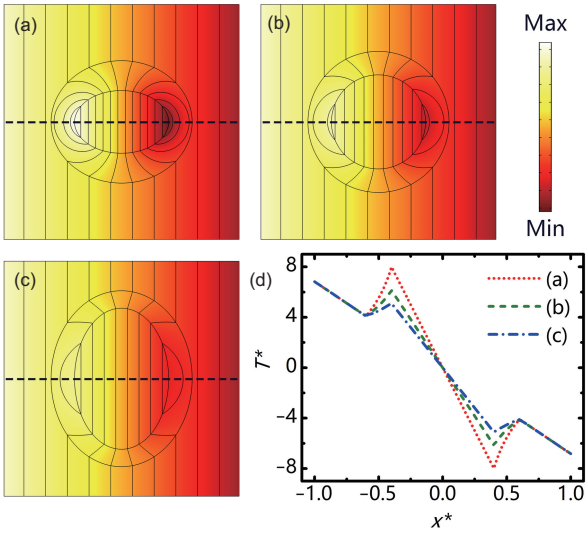

Figure 4 (Color online) (a)-(c) Simulations of the monolayer scheme with an isotropic thermal conductivity. (d) T^* as a function of x^*. Parameters: (a) $L_{c1} = 0.4$ and $\kappa_s/\kappa_c = -0.58$; (b) $L_{c1} = 0.5$ and $\kappa_s/\kappa_c = -1$; (c) $L_{c1} = 0.6$ and $\kappa_s/\kappa_c = -1.87$; and (a)-(c) $r_{s1}/r_{c1} = 1.5$ and $\kappa_c = \kappa_b$.

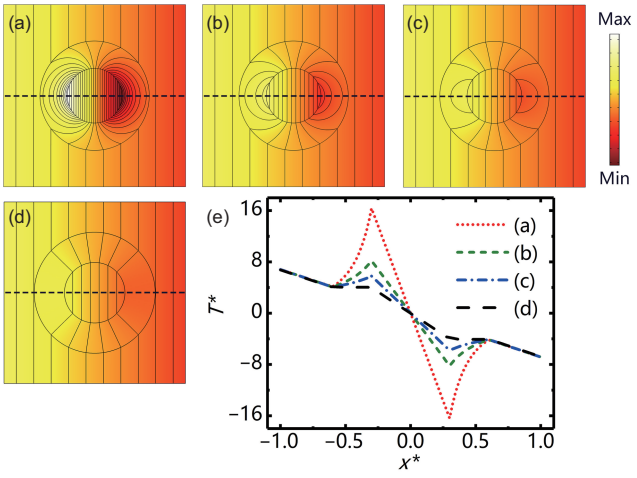

Figure 5 (Color online) (a)-(c) Simulations of the monolayer scheme with an anisotropic thermal conductivity. (d) Temperature distribution of the existing scheme based on transformation theory and $\eta \to r_s/r_c$. (e) T^* as a function of x^*. Parameters: (a) $\kappa_{srr}/\kappa_c = -0.5$; (b) $\kappa_{srr}/\kappa_c = -1$; (c) $\kappa_{srr}/\kappa_c = -2$; (d) $\kappa_{srr}/\kappa_c = (r + 100)/r$; and (a)-(d) $r_s/r_c = 2$ and $\kappa_c = \kappa_b$.

For the bilayer scheme with isotropic thermal conductivities, two coupling conditions (i.e., eqs. (27) and (28)) are available. Similar to the structures in Figures 4 and 5, those in Figure 6 also ensure that isotherms outside the shells are straight and those in the cores are denser, thereby realizing the effect of thermal concentrating. With the coupling condition of eq. (27), the efficiency changes continuously with κ_t/κ_c (Figure 3(b)). We further design a structure to display the concentrating efficiency when $\kappa_t/\kappa_c \to 0^-$ (Figure 6(a)). The coupling condition of eq. (28) can lead to an infinite efficiency. That is, $\eta \to +\infty$ when $\kappa_t/\kappa_c \to 0^-$ (Figure 6(b)) or $\kappa_t/\kappa_c \to -\infty$ (Figure 6(c)), and $\eta \to -\infty$ for $\kappa_t/\kappa_c \to 0^+$ (see Figure 6(d)) or $\kappa_t/\kappa_c \to +\infty$ (Figure 6(e)). As shown in Figure 6(f), the effect of thermal concentrating can be quantitatively observed.

6 Experimental suggestions

The coupling conditions require apparent negative thermal conductivities [46-50], which cannot happen spontaneously in experiments. To achieve the equivalent effect, we can resort to external heat sources (Figure 7(a)). According to the thermal uniqueness theorem [55, 56], as long as we realize the same boundary temperature distributions by adding external heat sources at the inner and outer boundaries of the shell, we can obtain the same temperature profiles. Since the central temperature gradient and heat flux in Figure 7(c) are almost the same as those in Figure 7(b), we prove that an apparent negative thermal conductivity can be effectively

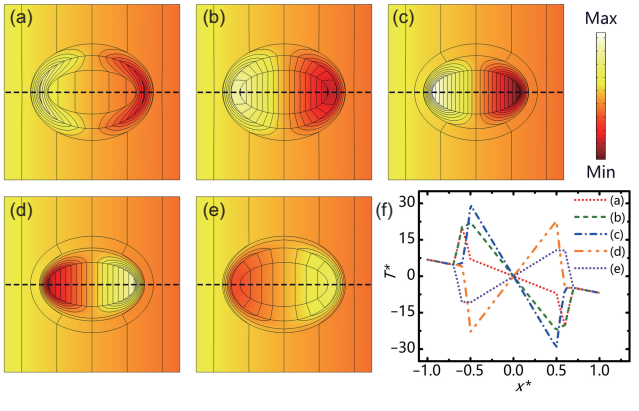

Figure 6 (Color online) (a)-(e) Simulations of the bilayer scheme with isotropic thermal conductivities. (f) T^* as a function of x^*. Parameters: (a) $\kappa_s/\kappa_c = 0.0826$ and $\kappa_t/\kappa_c = -0.05$; (b) $\kappa_s/\kappa_c = -1.14$ and $\kappa_t/\kappa_c = -0.05$; (c) $\kappa_s/\kappa_c = -0.175$ and $\kappa_t/\kappa_c = -10$; (d) $\kappa_s/\kappa_c = -0.122$ and $\kappa_t/\kappa_c = 15$; (e) $\kappa_s/\kappa_c = -2.83$ and $\kappa_t/\kappa_c = 0.05$; and (a)-(e) $r_{s1}/r_{c1} = 1.2$, $r_{t1}/r_{c1} = 1.4$, $L_{c1} = 1/3$, and $\kappa_c = \kappa_b$.

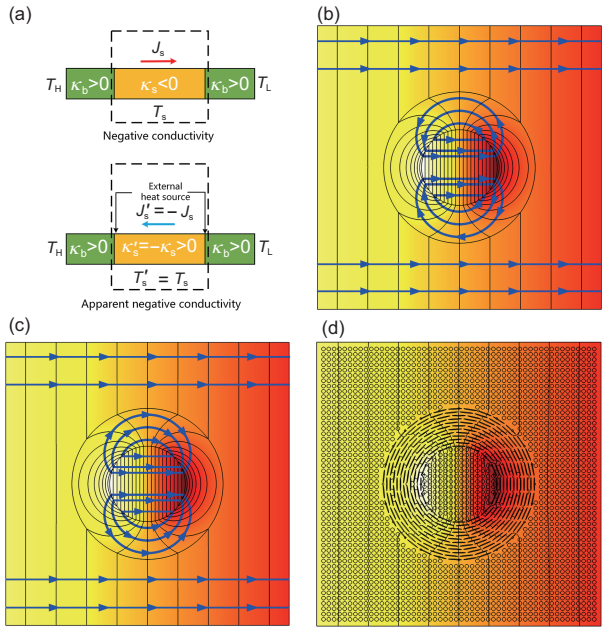

Figure 7 (Color online) Experimental suggestions. (a) Schematic diagram for realizing apparent negative conductivity. (b) Without temperature control. (c) Continuous temperature control. (d) Discrete point heat sources whose temperatures are shown in Tables 1 and 2. The core and background in (d) are a brass plate (109 W m^{-1} K^{-1}) drilled with 2116 air circles with a radius of 0.1 cm. The shell is drilled with 282 air ellipses with a major (or minor) semi-axis of 0.35 cm (or 0.02 cm). Other parameters: (b) and (d) κ_s = diag(23, 92) W m^{-1} K^{-1}; (c) κ_s = diag(−23, −92) W m^{-1} K^{-1}; and (b)-(d) r_c = 1 cm, r_s = 2 cm, $\kappa_c = \kappa_b$ = 46 W m^{-1} K^{-1}. The black lines and blue arrows in (b)-(d) denote isotherms and heat fluxes, respectively.

achieved by means of adding external heat sources. Then we design a structure as a feasible experimental suggestion (Figure 7(d)). We add a series of point heat sources at the inner and outer boundaries of the shell (Figure 7(d)). The detailed temperatures are presented in Tables 1 and 2, which can be experimentally controlled by adjusting the voltages of heaters and coolers according to eqs. (1) and (2) in ref. [55]. The required thermal conductivity can be realized by punching air holes on a brass plate (109 W m^{-1} K^{-1}), whose left and right edges are put into hot (313 K) and cold (273 K) sinks, respectively. To achieve the thermal conductivities of the core and background in Figure 7(b), 2116 air circles are drilled on the brass, leading to an effective thermal conductivity of 46 W m^{-1} K^{-1} (calculated by eq. (11) in ref. [57]). The shell region is composed of 282 air ellipses, leading to an effective thermal conductivity of diag(23, 92) W m^{-1} K^{-1} (calculated by eq. (11) in ref. [57]). By comparing the temperature distributions in Figure 7(b)-(d), we can confirm that the scheme in Figure 7(d) can realize the effect of Figure 7(b) in experiments.

7 Conclusion

To sum up, we break the upper limit for the concentrating efficiency of existing thermal concentrators by using coupling conditions of thermal conductivities. We first explore a monolayer scheme with an isotropic thermal conductivity, which can break the upper limit but is still limited by its geometric configuration. Then we consider a shell with an anisotropic thermal conductivity or add the second shell with an isotropic thermal conductivity as another degree of freedom, which renders the concentrating efficiency free from geometric configurations. Apparent negative thermal conductivities are required in these three schemes, which can be effectively realized by external energy or thermoelectric materials. Since negative permeability [58-60] and negative

Table 1 Temperatures of the point heat sources at the outer boundary of the shell in Figure 7(d)

Source	Temp. (K)	Source	Temp. (K)	Source	Temp. (K)	Source	Temp. (K)
1	293.00	7	282.30	13	293.00	19	303.70
2	290.24	8	282.69	14	295.76	20	303.30
3	287.68	9	283.78	15	298.32	21	302.22
4	285.45	10	285.45	16	300.55	22	300.55
5	283.78	11	287.68	17	302.22	23	298.32
6	282.69	12	290.24	18	303.30	24	295.76

Table 2 Temperatures of the point heat sources at the inner boundary of the shell in Figure 7(d)

Source	Temp. (K)	Source	Temp. (K)	Source	Temp. (K)	Source	Temp. (K)
1	293.00	7	250.34	13	293.00	19	335.67
2	281.96	8	251.79	14	304.04	20	334.21
3	271.67	9	256.05	15	314.33	21	329.95
4	259.83	10	259.83	16	323.17	22	323.17
5	256.05	11	271.67	17	329.95	23	314.33
6	251.79	12	281.96	18	334.21	24	304.04

electric conductivity [61] have been, respectively, revealed in static magnetic fields and dc current fields, it is promising to extend our results to these diffusive fields due to the similar equation forms (i.e., the Laplace equation). Moreover, the present theory is applicable not only for thermal concentrators with $\eta > 1$ but also for thermal invisible sensors with $\eta = 1$ [62, 63] and thermal cloaks with $\eta = 0$ (perfect cloaking) [64, 65] or $\eta < 1$ (imperfect cloaking) [66, 67]. Whether for concentrating, sensing, or cloaking, a typical feature is the undistorted background temperature distribution, so these schemes may provide insights into thermal camouflage [68] and illusion [69, 70] for misleading infrared detection. It is also promising to extend the related mechanisms towards multi-function and micro/nano-scale in the future.

This work was supported by the National Natural Science Foundation of China (Grant Nos. 11725521, and 12035004), and the Science and Technology Commission of Shanghai Municipality (Grant No. 20JC1414700). We are grateful to Prof. Chenping Zhu for his useful discussion.

1 C. Z. Fan, Y. Gao, and J. P. Huang, Appl. Phys. Lett. **92**, 251907 (2008).
2 T. Chen, C. N. Weng, and J. S. Chen, Appl. Phys. Lett. **93**, 114103 (2008).
3 J. P. Huang, *Theoretical Thermotics: Transformation Thermotics and Extended Theories for Thermal Metamaterials* (Springer, Singapore, 2020).
4 M. Maldovan, Nature **503**, 209 (2013).
5 S. Yang, J. Wang, G. Dai, F. Yang, and J. Huang, Phys. Rep. **908**, 1 (2021).
6 Y. Li, W. Li, T. Han, X. Zheng, J. Li, B. Li, S. Fan, and C. W. Qiu, Nat. Rev. Mater. **6**, 488 (2021), arXiv: 2008.07964.
7 W. Sha, M. Xiao, J. Zhang, X. Ren, Z. Zhu, Y. Zhang, G. Xu, H. Li, X. Liu, X. Chen, L. Gao, C. W. Qiu, and R. Hu, Nat. Commun. **12**, 7228 (2021).
8 G. X. Yu, Y. F. Lin, G. Q. Zhang, Z. Yu, L. L. Yu, and J. Su, Front. Phys. **6**, 70 (2011).
9 S. Guenneau, C. Amra, and D. Veynante, Opt. Express **20**, 8207 (2012).
10 T. Han, J. Zhao, T. Yuan, D. Y. Lei, B. Li, and C. W. Qiu, Energy Environ. Sci. **6**, 3537 (2013).
11 M. Moccia, G. Castaldi, S. Savo, Y. Sato, and V. Galdi, Phys. Rev. X **4**, 021025 (2014), arXiv: 1311.6119.
12 F. Chen, and D. Y. Lei, Sci. Rep. **5**, 11552 (2015).
13 Y. Li, X. Shen, J. Huang, and Y. Ni, Phys. Lett. A **380**, 1641 (2016).
14 A. M. Abdalla, S. Hossain, O. B. Nisfindy, A. T. Azad, M. Dawood, and A. K. Azad, Energy Convers. Manage. **165**, 602 (2018).
15 Q. Ji, G. Fang, and J. Liang, J. Phys. D-Appl. Phys. **51**, 315304 (2018).
16 G. Xu, X. Zhou, and Z. Liu, Int. Commun. Heat Mass Transfer **108**, 104337 (2019).
17 T. Li, C. Yang, S. Li, D. Zhu, Y. Han, and Z. Li, J. Phys. D-Appl. Phys. **53**, 065503 (2020).
18 Y. Li, H. Zhang, Z. Zhang, Z. Wang, and X. Xia, AIP Adv. **10**, 105214 (2020).
19 Y. Li, and H. Zhang, Chin. Phys. B **29**, 084401 (2020).
20 L. J. Xu, S. Yang, G. L. Dai, and J. P. Huang, ES Energy Environ. **7**, 65 (2020).
21 R. Hu, S. Huang, M. Wang, L. Zhou, X. Peng, and X. Luo, Phys. Rev. Appl. **10**, 054032 (2018).
22 S. Narayana, and Y. Sato, Phys. Rev. Lett. **108**, 214303 (2012).
23 R. S. Kapadia, and P. R. Bandaru, Appl. Phys. Lett. **105**, 233903 (2014).
24 C. Lan, B. Li, and J. Zhou, Opt. Express **23**, 24475 (2015), arXiv: 1505.03212.
25 T. Chen, C. N. Weng, and Y. L. Tsai, J. Appl. Phys. **117**, 054904 (2015).
26 R. Wang, L. Xu, Q. Ji, and J. Huang, J. Appl. Phys. **123**, 115117 (2018).
27 X. Shen, Y. Li, C. Jiang, Y. Ni, and J. Huang, Appl. Phys. Lett. **109**, 031907 (2016), arXiv: 1506.01532.
28 G. Xu, X. Zhou, and J. Zhang, Int. J. Heat Mass Transfer **142**, 118434 (2019).
29 L. Xu, S. Yang, and J. Huang, Phys. Rev. E **98**, 052128 (2018).
30 G. Fujii, and Y. Akimoto, Int. J. Heat Mass Transfer **159**, 120082 (2020).
31 Q. Ji, X. Chen, J. Liang, V. Laude, S. Guenneau, G. Fang, and M. Kadic, Int. J. Heat Mass Transfer **169**, 120948 (2021), arXiv: 2008.08928.
32 C. B. Hu, B. Liang, J. Yang, and J. C. Cheng, Sci. China-Phys. Mech. Astron. **64**, 244304 (2021).
33 X. Jia, Y. Li, Y. Zhou, M. Hong, and M. Yan, Sci. China-Phys. Mech. Astron. **62**, 964311 (2019).
34 R. Hu, S. Huang, M. Wang, X. Luo, J. Shiomi, and C. W. Qiu, Adv. Mater. **31**, 1807849 (2019).
35 G. Fujii, Y. Akimoto, and M. Takahashi, Appl. Phys. Lett. **112**, 061108 (2018).
36 G. Fujii, and Y. Akimoto, Appl. Phys. Lett. **115**, 174101 (2019).
37 G. Fujii, and Y. Akimoto, Int. J. Heat Mass Transfer **137**, 1312 (2019).
38 G. Fujii, and Y. Akimoto, Phys. Rev. E **102**, 033308 (2020).
39 B. Liu, L. Xu, and J. Huang, J. Appl. Phys. **129**, 065101 (2021).
40 R. Hu, S. Iwamoto, L. Feng, S. Ju, S. Hu, M. Ohnishi, N. Nagai, K. Hirakawa, and J. Shiomi, Phys. Rev. X **10**, 021050 (2020).
41 L. Xu, S. Yang, and J. Huang, Phys. Rev. Appl. **11**, 054071 (2019).
42 F. Sun, Y. Liu, Y. Yang, Z. Chen, and S. He, Opt. Express **27**, 33757 (2019).
43 F. Yang, B. Tian, L. Xu, and J. Huang, Phys. Rev. Appl. **14**, 054024 (2020).
44 H. Barati Sedeh, M. H. Fakheri, A. Abdolali, F. Sun, and Y. Ma, Phys. Rev. Appl. **14**, 064034 (2020).
45 L. J. Xu, and J. P. Huang, Sci. China-Phys. Mech. Astron. **63**, 228711 (2020).
46 Y. Gao, and J. P. Huang, Europhys. Lett. **104**, 44001 (2013), arXiv: 1309.5581.
47 M. Wegener, Science **342**, 939 (2013).
48 X. Y. Shen, and J. P. Huang, Int. J. Heat Mass Transfer **78**, 1 (2014).
49 S. Yang, L. Xu, and J. Huang, J. Appl. Phys. **125**, 055103 (2019).
50 L. Xu, and J. Huang, Chin. Phys. Lett. **37**, 080502 (2020).
51 G. W. Milton, *The Theory of Composites* (Cambridge University Press, Cambridge, 2002).
52 J. Y. Li, Y. Gao, and J. P. Huang, J. Appl. Phys. **108**, 074504 (2010).
53 X. Zheng, and B. Li, Phys. Rev. Appl. **13**, 024071 (2020), arXiv: 1911.05098.
54 J. Guo, X. N. Chen, Z. G. Qu, and Q. L. Ren, Int. J. Heat Mass Transfer **173**, 121244 (2021).
55 D. M. Nguyen, H. Xu, Y. Zhang, and B. Zhang, Appl. Phys. Lett. **107**, 121901 (2015), arXiv: 2110.10845.
56 L. J. Xu, and J. P. Huang, Chin. Phys. Lett. **37**, 120501 (2020).
57 S. Yang, L. J. Xu, R. Z. Wang, and J. P. Huang, Appl. Phys. Lett. **111**, 121908 (2017).
58 R. Mach-Batlle, A. Parra, J. Prat-Camps, S. Laut, C. Navau, and A. Sanchez, Phys. Rev. B **96**, 094422 (2017), arXiv: 1803.08013.
59 R. Mach-Batlle, A. Parra, S. Laut, N. Del-Valle, C. Navau, and A. Sanchez, Phys. Rev. Appl. **9**, 034007 (2018), arXiv: 1803.08009.
60 R. Mach-Batlle, M. G. Bason, N. Del-Valle, and J. Prat-Camps, Phys. Rev. Lett. **125**, 177204 (2020).
61 T. Chen, B. Zheng, Y. Yang, L. Shen, Z. Wang, F. Gao, E. Li, Y. Luo, T. J. Cui, and H. Chen, Light Sci. Appl. **8**, 30 (2019).

62 T. Yang, X. Bai, D. Gao, L. Wu, B. Li, J. T. L. Thong, and C. W. Qiu, Adv. Mater. **27**, 7752 (2015).
63 P. Jin, L. Xu, T. Jiang, L. Zhang, and J. Huang, Int. J. Heat Mass Transfer **163**, 120437 (2020).
64 Z. Zhu, X. Ren, W. Sha, M. Xiao, R. Hu, and X. Luo, Int. J. Heat Mass Transfer **176**, 121417 (2021).
65 L. Zhou, S. Huang, M. Wang, R. Hu, and X. Luo, Phys. Lett. A **383**, 759 (2019).
66 Y. Li, K. J. Zhu, Y. G. Peng, W. Li, T. Yang, H. X. Xu, H. Chen, X. F. Zhu, S. Fan, and C. W. Qiu, Nat. Mater. **18**, 48 (2019).
67 L. J. Xu, S. Yang, and J. P. Huang, Europhys. Lett. **131**, 24002 (2020).
68 R. Hu, W. Xi, Y. Liu, K. Tang, J. Song, X. Luo, J. Wu, and C. W. Qiu, Mater. Today **45**, 120 (2021).
69 S. Zhou, R. Hu, and X. Luo, Int. J. Heat Mass Transfer **127**, 607 (2018).
70 R. Hu, S. Zhou, Y. Li, D. Y. Lei, X. Luo, and C. W. Qiu, Adv. Mater. **30**, 1707237 (2018).

Appendix

A1 The relationship between undetermined coefficients in eq. (3)

According to the continuities of temperature and normal heat flux, we have

$$\begin{cases} T_{ci}|_{\rho_1=\rho_c} = T_{si}|_{\rho_1=\rho_c}, \\ T_{si}|_{\rho_1=\rho_s} = T_{bi}|_{\rho_1=\rho_s}, \\ \kappa_c \dfrac{\partial T_{ci}}{\partial \rho_1}\Big|_{\rho_1=\rho_c} = \kappa_s \dfrac{\partial T_{si}}{\partial \rho_1}\Big|_{\rho_1=\rho_c}, \\ \kappa_s \dfrac{\partial T_{si}}{\partial \rho_1}\Big|_{\rho_1=\rho_s} = \kappa_b \dfrac{\partial T_{bi}}{\partial \rho_1}\Big|_{\rho_1=\rho_s}. \end{cases} \tag{a1}$$

With eq. (3), we can express eq. (a1) as:

$$\begin{cases} A_{ci} = A_{si} + B_{si}\phi_i(\rho_c), \\ A_{si} + B_{si}\phi_i(\rho_s) = A_{bi} + B_{bi}\phi_i(\rho_s), \\ \kappa_c A_{ci} = \kappa_s \left[A_{si} + 2B_{si}/g(\rho_c) + B_{si}\phi_i(\rho_c)\right], \\ \kappa_s \left[A_{si} + 2B_{si}/g(\rho_s) + B_{si}\phi_i(\rho_s)\right] \\ \quad = \kappa_b \left[A_{bi} + 2B_{bi}/g(\rho_s) + B_{bi}\phi_i(\rho_s)\right]. \end{cases} \tag{a2}$$

To express $\phi_i(\rho_c)$ and $\phi_i(\rho_s)$ in a physical form, we define L_{ci} (or L_{si}) as the shape factor of the inner (or outer) boundary of the shell along the x_i axis,

$$L_{ci} = \frac{g(\rho_c)}{2} \int_{\rho_c}^{\infty} \left[\left(\rho_1 + r_{ci}^2\right) g(\rho_1)\right]^{-1} \mathrm{d}\rho_1, \tag{a3}$$

$$L_{si} = \frac{g(\rho_s)}{2} \int_{\rho_s}^{\infty} \left[\left(\rho_1 + r_{ci}^2\right) g(\rho_1)\right]^{-1} \mathrm{d}\rho_1, \tag{a4}$$

with definitions of $g(\rho_c) = \prod_i r_{ci}$ and $g(\rho_s) = \prod_i r_{si}$. With eqs. (a3) and (a4), we can further obtain

$$\phi_i(\rho_c) = \int_{\rho_c}^{\rho_c} \left[\left(\rho_1 + r_{ci}^2\right) g(\rho_1)\right]^{-1} \mathrm{d}\rho_1 = 0, \tag{a5}$$

$$\begin{aligned} \phi_i(\rho_s) &= \left(\int_{\rho_c}^{\infty} - \int_{\rho_s}^{\infty}\right) \left[\left(\rho_1 + r_{ci}^2\right) g(\rho_1)\right]^{-1} \mathrm{d}\rho_1 \\ &= 2L_{ci}/g(\rho_c) - 2L_{si}/g(\rho_s). \end{aligned} \tag{a6}$$

The shape factors satisfy $\sum_i L_{ci} = 1$ and $\sum_i L_{si} = 1$. For two dimensions, the shape factors can be further reduced to $L_{c1} = r_{c2}/(r_{c1}+r_{c2})$, $L_{c2} = r_{c1}/(r_{c1}+r_{c2})$, $L_{s1} = r_{s2}/(r_{s1}+r_{s2})$, and $L_{s2} = r_{s1}/(r_{s1}+r_{s2})$. According to the variables of $R = r_{s1}/r_{c1}$ and L_{c1} in Figure 1(b), we can determine the geometric parameters (r_{c1}, r_{c2}, r_{s1}, and r_{s2}) of a thermal concentrator, with the following relationships:

$$\begin{cases} r_{c2} = \dfrac{L_{c1}}{1-L_{c1}} r_{c1}, \\ r_{s1} = R r_{c1}, \\ r_{s2} = \sqrt{r_{s1}^2 - c^2} = \dfrac{\sqrt{R^2(1-L_{c1})^2 + 2L_{c1} - 1}}{1-L_{c1}} r_{c1}, \end{cases} \tag{a7}$$

where the core-shell structure is confocal and c is the half focal length, i.e., $c^2 = r_{c1}^2 - r_{c2}^2 = \frac{1-2L_{c1}}{(1-L_{c1})^2} r_{c1}^2$.

A2 The relationship between undetermined coefficients in eq. (12)

The system (Figure 2(a)) has the corresponding boundary conditions,

$$\begin{cases} T_c|_{r=r_c} = T_s|_{r=r_c}, \\ T_s|_{r=r_s} = T_b|_{r=r_s}, \\ \kappa_c \dfrac{\partial T_c}{\partial r}\Big|_{r=r_c} = \kappa_{srr} \dfrac{\partial T_s}{\partial r}\Big|_{r=r_c}, \\ \kappa_{srr} \dfrac{\partial T_s}{\partial r}\Big|_{r=r_s} = \kappa_b \dfrac{\partial T_b}{\partial r}\Big|_{r=r_s}. \end{cases} \tag{a8}$$

The substitution of eq. (12) into eq. (a8) yields

$$\begin{cases} A_c r_c = A_s r_c^{d_{s1}} + B_s r_c^{d_{s2}}, \\ A_s r_s^{d_{s1}} + B_s r_s^{d_{s2}} = A_b r_s + B_b r_s^{-1}, \\ \kappa_c A_c = \kappa_{srr}\left(d_{s1} A_s r_c^{d_{s1}-1} + d_{s2} B_s r_c^{d_{s2}-1}\right), \\ \kappa_{srr}\left(d_{s1} A_s r_s^{d_{s1}-1} + d_{s2} B_s r_s^{d_{s2}-1}\right) = \kappa_b\left(A_b - B_b r_s^{-2}\right). \end{cases} \tag{a9}$$

A3 Three-dimensional monolayer scheme with an anisotropic thermal conductivity

The tensorial thermal conductivity of the shell can be expressed in the spherical coordinate system (r, θ, ϕ) as $\overleftrightarrow{\kappa}_s = \mathrm{diag}\left(\kappa_{srr}, \kappa_{s\theta\theta}, \kappa_{s\phi\phi}\right)$. For simplicity, we assume a axial symmetry with $\kappa_{s\theta\theta} = \kappa_{s\phi\phi}$. Therefore, thermal conduction is independent of ϕ, which is dominated by

$$\frac{1}{r^2}\frac{\partial}{\partial r}\left(r^2 \kappa_{srr} \frac{\partial T}{\partial r}\right) + \frac{1}{r\sin\theta}\frac{\partial}{\partial \theta}\left(\sin\theta \kappa_{s\theta\theta} \frac{\partial T}{r \partial \theta}\right) = 0. \tag{a10}$$

The temperature distributions in the core T_c , shell T_s, and background T_b can be written as:

$$\begin{cases} T_c = A_c r\cos\theta, \\ T_s = \left(A_s r^{h_{s1}} + B_s r^{h_{s2}}\right)\cos\theta, \\ T_b = \left(A_b r + B_b r^{-2}\right)\cos\theta, \end{cases} \tag{a11}$$

with definitions of $h_{s1} = \left(-1 + \sqrt{1 + 8\kappa_{s\theta\theta}/\kappa_{srr}}\right)/2$ and $h_{s2} = \left(-1 - \sqrt{1 + 8\kappa_{s\theta\theta}/\kappa_{srr}}\right)/2$. By substituting eq. (a11) into the boundary conditions of eq. (a8), we can obtain

$$\begin{cases} A_c r_c = A_s r_c^{h_{s1}} + B_s r_c^{h_{s2}}, \\ A_s r_s^{h_{s1}} + B_s r_s^{h_{s2}} = A_b r_s + B_b r_s^{-2}, \\ \kappa_c A_c = \kappa_{srr}\left(h_{s1} A_s r_c^{h_{s1}-1} + h_{s2} B_s r_c^{h_{s2}-1}\right), \\ \kappa_{srr}\left(h_{s1} A_s r_s^{h_{s1}-1} + h_{s2} B_s r_s^{h_{s2}-1}\right) = \kappa_b\left(A_b - 2B_b r_s^{-3}\right). \end{cases} \tag{a12}$$

We can calculate A_c, A_s, B_s, and B_b with eq. (a12). By taking $B_b = 0$, we can further derive

$$\kappa_b = \frac{h_{s1}\left(\kappa_c - h_{s2}\kappa_{srr}\right) - h_{s2}\left(\kappa_c - h_{s1}\kappa_{srr}\right) f^{(h_{s1}-h_{s2})/3}}{\kappa_c - h_{s2}\kappa_{srr} - \left(\kappa_c - h_{s1}\kappa_{srr}\right) f^{(h_{s1}-h_{s2})/3}}\kappa_{srr}, \tag{a13}$$

with a definition of $f = r_c^3/r_s^3$. The concentrating efficiency is

$$\eta = \frac{A_c}{A_b} = \frac{\left(h_{s1} - h_{s2}\right)\kappa_{srr} f^{(h_{s1}-1)/3}}{\kappa_c - h_{s2}\kappa_{srr} - \left(\kappa_c - h_{s1}\kappa_{srr}\right) f^{(h_{s1}-h_{s2})/3}}. \tag{a14}$$

For an isotropic case with $h_{s1} = 1$ and $h_{s2} = -2$, eq. (a14) can be simplified as:

$$\eta = \frac{3\kappa_{srr}}{\kappa_c + 2\kappa_{srr} - \left(\kappa_c - \kappa_{srr}\right) f}, \tag{a15}$$

which has the same form as eq. (7) in sect. 2.

We can also derive two coupling conditions for $\kappa_c = \kappa_b$,

$$h_{s1}\kappa_{srr} = \kappa_c, \tag{a16}$$

$$h_{s2}\kappa_{srr} = \kappa_c. \tag{a17}$$

Eqs. (a16) and (a17) can also be unified as:

$$2\kappa_{srr}\kappa_{s\theta\theta} - \kappa_c\kappa_{srr} = \kappa_c^2. \tag{a18}$$

When eq. (a18) is satisfied, eq. (a14) can be reduced to

$$\eta = f^{-(1-\kappa_c/\kappa_{srr})/3} = \left(r_s/r_c\right)^{1-\kappa_c/\kappa_{srr}}, \tag{a19}$$

which has the same form as two dimensions (i.e., eq. (19)). Therefore, the minimum value $\eta \to 0$ occurs with $\kappa_{srr}/\kappa_c \to 0^+$, and the maximum value $\eta \to \infty$ occurs with $\kappa_{srr}/\kappa_c \to 0^-$. Moreover, we can find $\eta \to r_s/r_c$ when $\kappa_{srr}/\kappa_c \to \pm\infty$. If we consider an isotropic and nontrivial shell with $\kappa_{srr}/\kappa_c = 1/h_{s2} = -1/2$, the concentrating efficiency becomes $\eta = r_s^3/r_c^3$, which also agrees with the three-dimensional conclusion in sect. 2.